Effects of the 2018 Martian Global Dust Storm on Boundary Positions in the Induced Magnetosphere

Catherine E. Regan[1,2,3] , Andrew J. Coates[1,2] , Mark Lester[4], Anne Wellbrock[1,2] , Geraint H. Jones[1,2] ,
Beatriz Sánchez-Cano[4] , Philippe Garnier[5], Louisa J. Preston[1,2], František Němec[6] , Václav Linzmayer[6], Rudy A. Frahm[7], and
Mats Holmström[8]

[1] Mullard Space Science Laboratory, Department of Space and Climate Physics, University College London, UK; catherine.regan@mail.wvu.edu
[2] Centre for Planetary Sciences at UCL and Birkbeck, London, UK
[3] Department of Physics and Astronomy, West Virginia University, WV, USA
[4] School of Physics and Astronomy, University of Leicester, UK
[5] IRAP, Toulouse, France
[6] Faculty of Mathematics and Physics, Charles University, Czech Republic
[7] Southwest Research Institute, TX, USA
[8] Swedish Institute of Space Physics, Kiruna, Sweden

Abstract

Global dust storms at Mars have a significant impact on the atmosphere and ionosphere, but only recently has their impact on the magnetosphere been investigated. The 2018 global dust storm at Mars was the first global event following the arrival of the Mars Atmosphere and Volatile EvolutioN mission at Mars, providing additional data to that of Mars Express observing how plasma boundaries (the bow shock and induced magnetospheric boundary (IMB)) varied over the storm duration. Applying 2D boundary models to spacecraft crossings, we find that the variability of both boundaries increases due to the storm onset and continues after surface conditions have returned to normal. While the bow shock shows no influence from the crustal magnetic fields in the southern hemisphere of Mars, the IMB dips here, the opposite of its normal bulging behavior. This is consistent with the signature found during the 2007 global dust storm. We suggest this signature is due to a decrease in ionospheric pressure in this area from the transport of ionized particles down crustal magnetic field lines toward the surface of Mars.

Unified Astronomy Thesaurus concepts: Mars (1007); Planetary magnetospheres (997)

1. Introduction

The environment of Mars is complex, with the coupling between the surface, atmosphere, ionosphere, and magnetosphere being an important topic in understanding this system. One area that is not fully understood is how atmospheric conditions and events potentially impact the wider system out into the magnetosphere. C. Regan et al. (2024) analyzed the impact of the 2007 global scale dust storm on boundaries in the induced magnetosphere. We continue this avenue of research by using the same techniques on the 2018 global scale dust storm in order to understand if the system responds the same way to all global dust storms.

1.1. Mars's Induced Magnetosphere

Mars's magnetosphere is induced as the solar wind interacts directly with its exosphere and ionosphere, due to the lack of dipole magnetic field. As the supersonic solar wind is deflected around the planet, it slows to subsonic speeds at a boundary known as the bow shock. It is characterized by an enhancement of magnetic field draping and an increase in plasma temperature and density. At the subsolar and terminator points, the bow shock is located approximately 0.58–1.6 R_M from the surface of Mars, where $R_M = 3390$ km, the radius of Mars (C. Bertucci et al. 2011). The location of the bow shock varies over the solar cycle (7%) and the Martian year (11%) (B. Hall et al. 2019) and

on shorter timescales due to solar events such as coronal mass ejections (P. Garnier et al. 2022a). Crossing of the bow shock leads to the magnetosheath, which is populated by high-density and energy decelerated solar wind plasma.

The lower boundary of the magnetosheath is the induced magnetospheric boundary (IMB), also referred to as the magnetic pile-up boundary. Similar to Earth's magnetopause, the IMB forms a barrier to the solar wind flow and is a sharp, distinct discontinuity separating the solar wind population from the planetary plasma population at Mars. It is characterized by an increase in magnetic field magnitude and total electron density and a decrease in electron temperature and solar wind ion density. It is located on average at 0.33–0.45 R_M at the subsolar and terminator points (C. Bertucci et al. 2011). N. Edberg et al. (2008, 2009) observed that the IMB bulges in the southern hemisphere over the crustal magnetic fields, as trapped plasma here increases pressure on the boundary, pushing it to higher altitudes compared to elsewhere on Mars.

1.2. Global Dust Storms

Mars experiences a dust season every Mars year, peaking during the southern hemispheric summer, where regional storms are extremely common. Dust is also transported at Mars daily, through saltation, winds, and dust devils. Dust transportation is an important driver for the climate system of Mars and has the power to influence atmospheric temperature. Occasionally during dust storm season, regional storms may grow and/or merge to form a storm system that covers the entire surface—a global dust storm. These last

Table 1
Development of the 2018 Global Dust Storm, from D. M. Kass et al. (2019),
A. Sánchez-Lavega et al. (2019), L. Montabone et al. (2020), L. Rossi et al.
(2021)

L_S (deg)	Earth Date, 2018	Storm Phase
176.0	May 15	Dust lifting begins
189.2	Jun. 7	Dust elevated to 40–60 km
194.9	Jun. 17	Storm becomes global
197.3	Jun. 21	Storm within a storm, temperatures exceeded 225 K
213.3	Jul. 18	Mature phase ends
255.0	Sep. 22	Onset of decay phase
257.0	Sep. 25	Regional dust event in southern pole region
270.0	Oct. 16	Temperatures and dust levels back to normal, nondusty conditions at the surface

occurred in 2018, 2007, and 2001, and it is not fully understood why they occur in some Mars years and not others. The 2007 global dust storm had a significant impact on the Martian atmosphere and ionosphere, increasing neutral temperatures to 240 K (D. M. Kass et al. 2014) and water vapor densities up to 10^{10} cm^{-3} at altitudes of 80 km (A. A. Fedorova et al. 2018). Hydrogen escape from Mars increased (M. S. Chaffin et al. 2014), and the ionosphere was seen to bulge at the beginning of the storm (N. Venkateswara Rao et al. 2019). A study on the impact of this storm was conducted by C. Regan et al. (2024) using data from Mars Express (MEx), finding that the variability of the bow shock and IMB position increases due to the storm. In addition, they found that the IMB, which usually bulges over crustal fields in the southern hemisphere (N. Edberg et al. 2008), becomes depressed over these regions. This signature had not been seen before at Mars.

1.2.1. 2018 Global Storm

The most recent global dust storm at Mars (at the time of writing) occurred in 2018 (Mars Year 34) during dust season. This was the first global dust storm of the Mars Atmosphere and Volatile EvolutioN mission (MAVEN, NASA; B. M. Jakosky et al. 2015), and the second of MEx (ESA; A. Cardesin-Moinelo et al. 2024). Dust lifting began at solar longitude (L_S) 176° (May 15; L. Rossi et al. 2021) and became global a month later at L_S 194°.9 (June 17; D. M. Kass et al. 2019). The storm system had multiple growth phases during its lifetime, in addition to a "storm within a storm" occurring at L_S 197°.3 (June 21; L. Montabone et al. 2020). At the storm's peak, dust was lifted up to altitudes of 80 km, wind speeds reached 200 m s^{-1}, and temperatures rose to 200 K (D. M. Kass et al. 2019; K. J. Roeten et al. 2022). The decay phase of the storm was initiated at L_S 255° (September 22) and surface conditions returned to normal at L_S 270° (October 16), where temperature and dust levels were back to normal, nondusty conditions at the surface, as determined by the Curiosity rover (L. Rossi et al. 2021). A summary of the storm development is shown in Table 1.

On the surface, the dust storm caused incident UV solar radiation to drop by 97%, and the diurnal range of air temperatures decreased by 40–60 K (from 70–90 K to 30–35 K) as measured by the Curiosity rover (S. D. Guzewich

et al. 2019). Atmospheric composition was altered, with CO_2^+, CO_2, and Ar densities increasing, O_2^+, N_2, and He remaining constant, and O^+, CO, and O densities decreasing (A. Farahat et al. 2021; J. F. Qin et al. 2022). Both MAVEN and the ExoMars Trace Gas Orbiter found water abundance at high altitudes (A. A. Fedorova et al. 2020; D. D. Niu et al. 2021), and it was estimated that hydrogen-deuterium oxide, the semiheavy isotope of water, was 40% more abundant during this Mars year in comparison to non-global-storm Mars years, indicating a large flux of water escape (L. Rossi et al. 2021). Moving to the ionosphere, the peak density was not found to be significantly impacted due to the storm, but the altitude of the peak ionospheric layer lifted from 130 to 150 km, seen in both MAVEN (M. Felici et al. 2020; V. Mukundan et al. 2021) and MEx (K. Peter et al. 2023) data. The response of the ionosphere in the southern hemisphere was delayed, with the ionospheric layer density altitude there peaking a few weeks after the northern hemisphere (M. Felici et al. 2020; V. Mukundan et al. 2021). Studies of regional dust storms have shown that the ionosphere is coupled in its response—during events in 2022 June–July, MAVEN found the M2 and M1 layers' (main and secondary layer of electron density peaks with altitude) both rose by the same amount (M. Felici et al. 2024). At the time of writing, there has been no research on the impact of the 2018 global dust storm on the induced magnetosphere of Mars. We use data from two satellites at Mars, MEx and MAVEN, to identify boundary crossings of the bow shock and IMB, which are then modeled using a 2D empirical boundary model over the study period before, during, and after the 2018 global dust storm.

2. Methodology

We follow similar methodology to that outlined in C. Regan et al. (2024), with the addition of data from MAVEN. We summarize the data products and models used below.

2.1. Instrumentation

To identify crossings of the bow shock and IMB, we use data collected by the MEx and MAVEN missions. MEx was launched by the European Space Agency in 2003 and began science operations in 2004. It continues to be operational (at the time of writing) after 21 Earth years of scientific return. NASA's MAVEN mission was launched in 2013, and began operations in 2014, giving nearly 10 yr of return (at the time of writing). We use data from the Analyzer of Space Plasmas and Energetic Atoms (ASPERA-3) instrument on board MEx (S. Barabash et al. 2006). It contains four instruments: two Energetic Neutral Atom instruments, an Electron Spectrometer (ELS), and an Ion Mass Analyzer (IMA). ELS can measure electrons with energies up to 20 keV q^{-1} and has full azimuthal angular coverage, with 16 nodes covering 22°.5 each. IMA is a stand-alone instrument mounted on the body and is a spherical electrostatic analyzer and collimeter system. It also has 16 nodes, each with a field of view of 22°.5, and can measure ions up to 30 keV q^{-1}. We use multiple instruments on board MAVEN; the Solar Wind Ion Analyzer (SWIA), Solar Wind Electron Analyzer (SWEA), and Magnetometer (MAG). This suite of instruments help to address the main science objectives of MAVEN, which are to study the interactions of the Sun and solar wind with Mars's magnetosphere (B. M. Jakosky et al. 2015). SWIA measures ions with
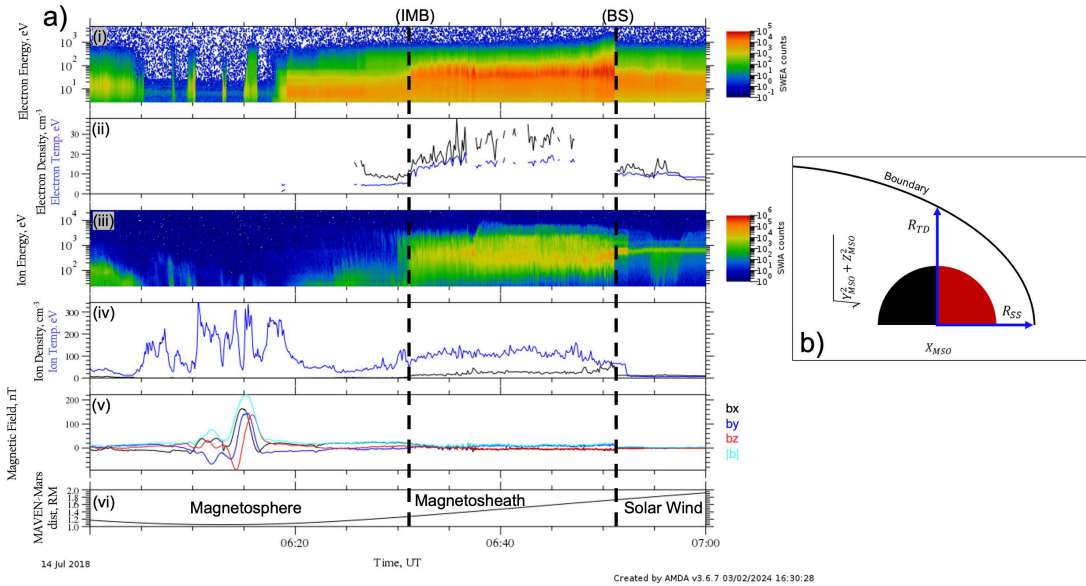
Figure 1. (a) MAVEN crossings of the induced magnetospheric boundary (IMB) and the bow shock (BS) on 2018 July 14. (i)–(ii) Electron energy, density, and temperature from SWEA; (iii)–(iv) ion energy, density, and temperature from SWIA; (v) magnetic field components and magnitude from MAG; (vi) MAVEN altitude over Mars in Mars radii. (b) Terminator and subsurface distances to boundaries from Mars in Mars Solar Orbital coordinates.

electrostatic deflectors, providing a $360° \times 90°$ field of view of ions ranging from 5 eV to 25 keV (J. S. Halekas et al. 2015). SWEA can measure electrons with energies between 3 and 4600 eV and is mounted at the end of a boom providing a field of view across 80% of the sky with a $20°$ resolution (D. L. Mitchell et al. 2016). MAG is composed of two independent triaxial fluxgate magnetometer sensors and provides magnetic field measurements with a resolution of 0.008 nT (J. Connerney et al. 2015).

2.2. Boundary Identification

We used visual identification of a boundary crossing of the bow shock and IMB by MEx to produce a catalog of crossings during our study period of 2018 April 1–November 30. For MAVEN, we used a catalog developed by V. Linzmayer et al. (2024) from an automatic detection algorithm that detects a boundary crossing when MAVEN crosses from one region to another, based on an automatic region detection algorithm from F. Němec et al. (2020). There were some gaps in this catalog during our study period due to threshold conditions not being met, so these gaps were filled with boundary identification by eye. An example of MAVEN boundary crossings is shown in Figure 1(a), and a MEx example can be seen in Figure 1 of C. Regan et al. (2024).

Using MEx, we used ELS data as our main method of identification as it has the highest resolution of the ASPERA-3 instruments. A sharp, distinct drop in the electron energy from approximately $10^{2.5}$ to $10^{1.5}$ eV and counts from over 10^2 to less than 10^1 mark an outbound bow shock crossing. Based on the resolution of ELS and the uncertainty associated with the spatial scale of the bow shock thickness (S. Burne et al. 2021), bow shock crossings have an uncertainty of ±32 s (S. Barabash et al. 2006). This is comparable to methods used in D. Vignes et al. (2000), N. Edberg et al. (2008), and B. Hall et al. (2016). For an outbound crossing of the IMB, electron populations increase from low energies up to 10^3 eV (C. Bertucci et al. 2011) with an increase in counts. The signatures of heavy ions disappear and protons are detected. Based on the lower resolution of IMA, we

primarily use ELS to identify an IMB crossing but use the protons and heavy ions as a supplementary data set where crossings were uncertain in ELS data. With MAVEN, the SWEA, SWIA, and MAG instruments are all used to detect boundary crossings. When traveling outbound, the bow shock is identified by a sharp decrease in electron energy spectra and counts, coincident with a drop in density and temperature. Ions also show a drop in density and temperature, with energy spectra also dropping. In the magnetic field, there is a sharp increase in values when compared to the magnetic field strength in the solar wind. Occasionally the ion and magnetic field values do not show a rapid change, but rather change over a few minutes. In these cases we use the electron data to mark a bow shock crossing to be consistent with the identification method used for MEx. Outbound IMB crossings are identified by an increase in electron and ion density and temperature, and a decrease in the magnetic field strength. Similarly to the bow shock, we take the electron data as the main indicator of a boundary crossing.

2.3. Boundary Modeling

To compare boundary crossings over the study period, we use a 2D empirical boundary model following methodology by D. Vignes et al. (2000), J. G. Trotignon et al. (2006), N. Edberg et al. (2008), and C. Regan et al. (2024). We calculate the terminator ($R_{\rm TD}$) and subsolar ($R_{\rm SS}$) distances for each crossing using Equations (1)–(2), where L is the semilatus rectum (Equation (3)) in polar coordinates of each crossing (r, θ), e is the boundary eccentricity, and x_0 is the conic focus. These distances are visualized in Figure 1(b).

$$R_{\rm TD} = \sqrt{L^2 + (e^2 - 1)x_0^2 + 2eLx_0}, \qquad (1)$$

$$R_{\rm SS} = x_0 + L(1 + e)^{-1}, \qquad (2)$$

$$L = r(1 + e\cos\theta). \qquad (3)$$

There are a range of values used for e and x_0 (Table 2). We use the constants provided by N. Edberg et al. (2008) for consistency with the 2007 global storm study, but the influence of using different constants is discussed in Section 3.1.
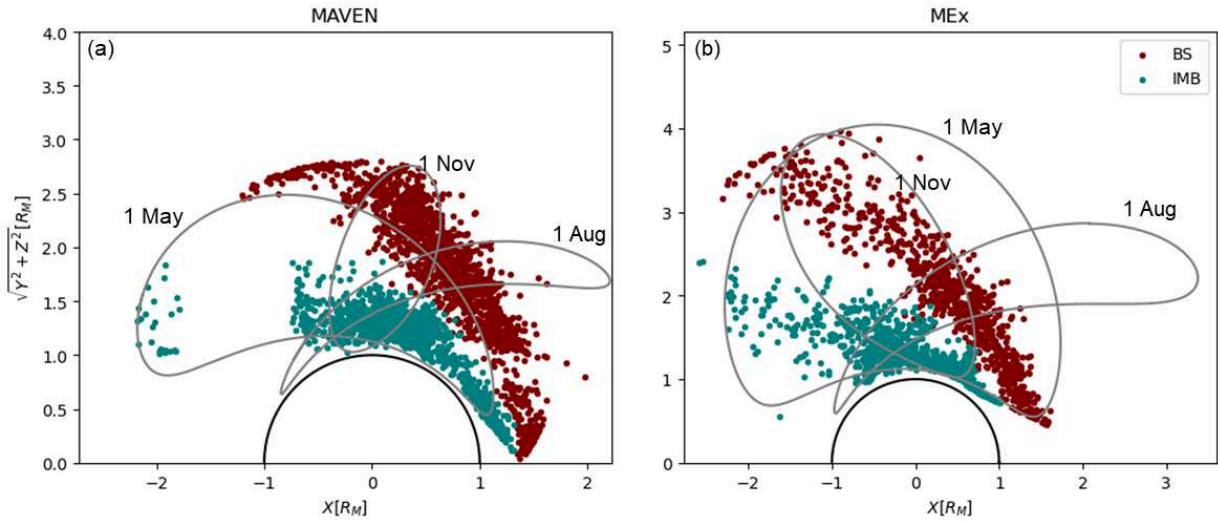
Figure 2. Bow shock (BS) and IMB crossings from (a) MAVEN and (b) Mars Express from 2018 April 1 to November 30, in rotated MSO coordinates. Single orbits from 00:00 on May 1, August 1, and November 1 annotated in gray.

Table 2
Bow Shock and IMB Constants for Eccentricity and Conic Focus

Bow Shock		
References	Eccentricity, e	Conic Focus, x_0 (R_M)
M. Wang et al. (2020)	1.05	0.5–0.8
B. Hall et al. (2019)	1.006	0.78
X. Fang et al. (2017)	0.872	0.42
N. Edberg et al. (2008)	1.05 ± 0.04	0.55 ± 0.12
J. G. Trotignon et al. (2006)	1.026 ± 0.002	0.6
D. Vignes et al. (2000)	1.03 ± 0.01	0.64 ± 0.02
IMB		
References	Eccentricity, e	Conic Focus, x_0 (R_M)
N. Edberg et al. (2008)	0.92 ± 0.03	0.86 ± 0.11
J. G. Trotignon et al. (2006)	0.77 ± 0.01	0.64 ± 0.01
D. Vignes et al. (2000)	0.90 ± 0.01	0.78 ± 0.01

Conducting analysis using the terminator distance removes the influence of the solar zenith angle on boundary positions and enables comparisons to be made between crossings. Rather than assuming a constant solar wind aberration angle of 4°, we calculate the exact aberration angle to rotate crossings about the Z-axis in Mars Solar Orbital (MSO) coordinates. We use model solar wind data (discussed later) and the Mars orbital velocity to calculate the angle for each crossing.

3. Results

From 2018 April 1 to November 30 there are 2399 total bow shock crossings (805 MEx, 1594 MAVEN) and 2321 total IMB crossings (782 MEx, 1539 MAVEN). Looking at dayside crossings only (where $X_{MSO} \geqslant 0$), this reduces to 2010 bow shock (580 MEx, 1430 MAVEN) and 1487 IMB (305 MEx, 1182 MAVEN) crossings. There are two data gaps present in the ASPERA-3 data during the study period; from April 13 to 27 there were no science operations on MEx due to the implementation of a gyroless mode, and from November 19 to 30 the instrument had to be turned off due to overheating (M. Holmström, personal communication). The distribution of the crossings used in this study is shown in Figure 2. Example

spacecraft orbits over the study period are plotted showing the orbit evolution over time. The MAVEN crossings are mostly on the dayside as the Linzmayer algorithm only identifies crossings on the dayside of Mars (based on the algorithm parameters). Nightside crossings from MAVEN have been identified by eye where there is a gap in the algorithm for completeness. MEx crossings are limited in the subsolar region due to the spacecraft's orbit over the study period. The apparent flattening at the largest distance of the bow shock in MAVEN data seen in the red dots grouped from −1 to 0 X and 2.5–3 $\sqrt{Y^2 + Z^2}$ in Figure 2(a) is an orbital effect.

3.1. Variability over Time

Following methodology from C. Regan et al. (2024), we remove any variation due to the change in the Sun–Mars distance over our study period by multiplying the modeled values by $r^{2.02}$, where r is the heliocentric distance, assuming a relationship with the dynamic pressure to the power of 2.02 as estimated by B. Hall et al. (2019) as the power law index of the variability. We use this for both boundaries for consistency with C. Regan et al. (2024) and assuming coupling between the bow shock and IMB. We focus on the dayside crossings of both boundaries, as variability of both increase past the terminator point and onto the nightside of the planet. The fitted subsolar and terminator distances for dayside crossings of both boundaries can be seen in Figures 3–4. Panel (a) in both figures shows the absolute value of the subsolar (Figure 3) and terminator (Figure 4) distances taken from Equations (2), (1). Figure 3(b) shows the variation in the Sun–Mars distance over the study period, which is then used to remove any influence of this variation, leaving the corrected values of subsolar and terminator distances in Figure 3(c). There is an uncertainty of ±20.4 km, taken from B. Hall et al. (2019), using the value calculated for Mars Year 28 (2007), which also experienced a global scale dust storm. This uncertainty is determined by the standard error on the fit parameters used as inputs for the boundary model.

For both the bow shock and the IMB, values begin scattered and then group together, forming a negative slope (the
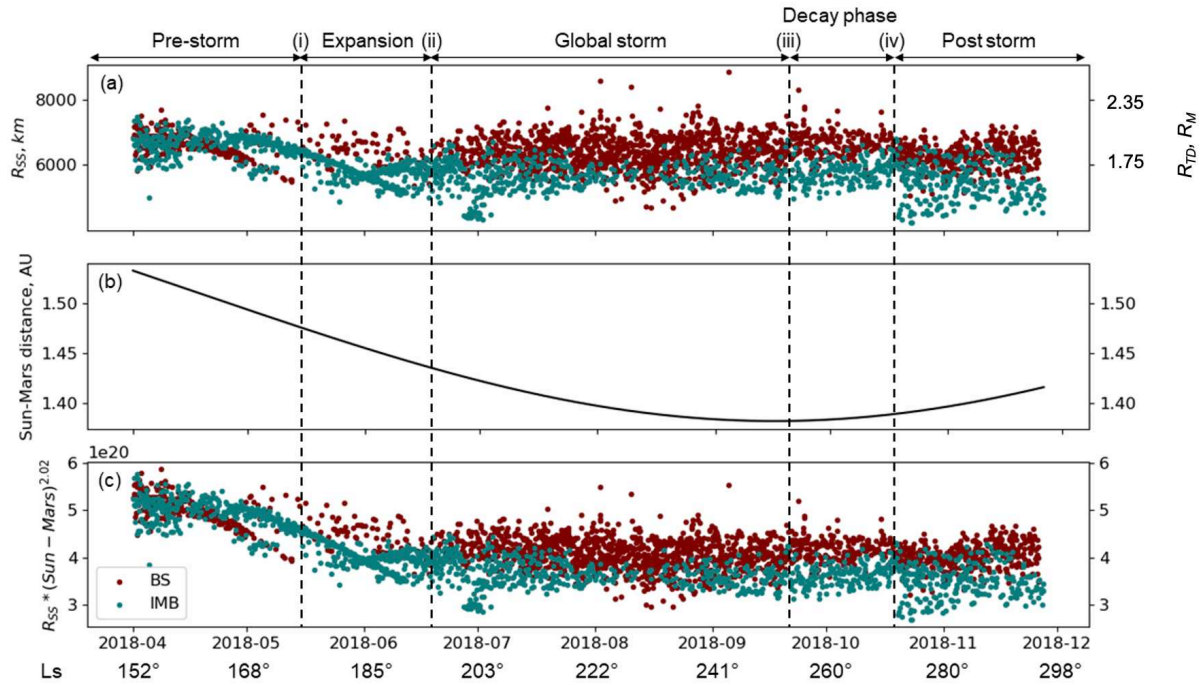
Figure 3. Dayside crossings from 2018 April 1 to November 30: (a) fitted subsolar distances (Equation (2)) for the bow shock (red) and IMB (blue), (b) distance between the Sun and Mars, and (c) fitted normalized subsolar distances taking into account the Sun–Mars distance in arbitrary units. Distances are measured from the center of Mars. Storm phases are overplotted as vertical lines where (i) dust lifting begins, (ii) the storm becomes global, (iii) the decay phase begins, and (iv) surface conditions return to normal (Table 1).
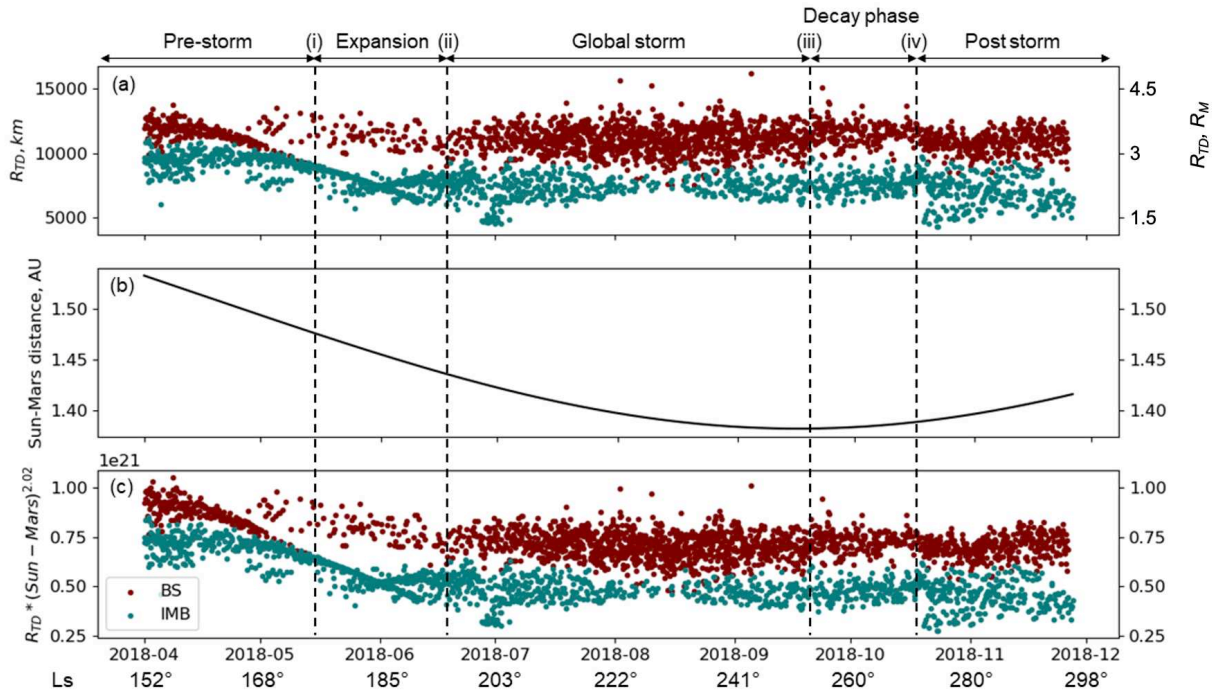
Figure 4. Dayside crossings from 2018 April 1 to November 30 for terminator distances (Equation (1)). Features are the same as described for Figure 3.

boundary moving toward the planet surface) moving into the expansion phase of the storm. As the storm becomes global at line (ii) in Figures 3 and 4, subsolar and terminator distances become more scattered, and this continues to the end of the study period. This strong grouping of values from April to June is a feature of the MAVEN crossings and is not seen in the MEx crossings. Removing the influence of the Sun–Mars

distance (Figures 3(c) and 4(c)) results in a steeper gradient of values during the prestorm and expansion phase. After the storm goes global there is no strong influence of the Sun–Mars distance, as Mars reaches perihelion. However, the boundaries remain closer to Mars after the expansion than at prestorm distances. Prior to the storm going global on June 17 (line (ii)), fitted subsolar and terminator distances have very constrained
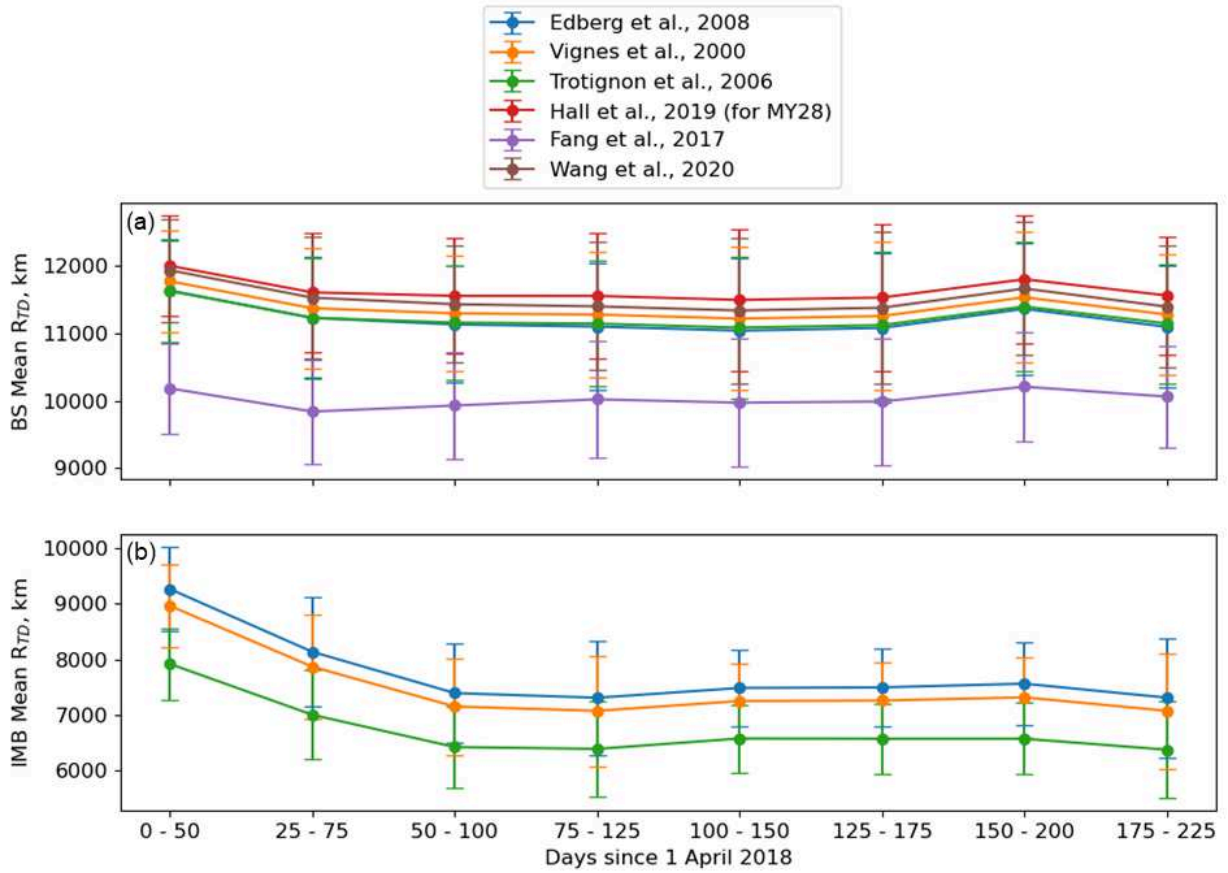
Figure 5. Comparison of different boundary models listed in Table 2 and resultant rolling means of the bow shock (a) and induced magnetospheric boundary (b) where the mean terminator distance is calculated every 50 days since the start of the study period, with 25 day intervals. Error bars indicate the standard deviation of results.

distributions, particularly for the IMB where the peaks of a bimodal distribution cross over each other at the start of June. This is an orbital effect of MAVEN, with these crossings having very similar X-coordinates and solar zenith angles. For both boundaries, there is more variability in fitted values after the storm goes global at line (ii). This continues after the surface conditions return to normal on October 16 (line (iv)). There is some overlap in subsolar distance values for the bow shock and IMB. This is due to the subsolar point being more difficult to constrain to represent the boundary shape. For this reason, we focus on the terminator distance for our detailed analysis.

We also investigated how different boundary models would alter our results. We looked at a rolling mean of the terminator distance for both boundaries using different eccentricity and conic focus values outlined in Table 2. The results are shown in Figure 5 for the (a) bow shock and (b) IMB. For the bow shock, the D. Vignes et al. (2000), J. G. Trotignon et al. (2006), N. Edberg et al. (2008), B. Hall et al. (2019), and M. Wang et al. (2020) models are similar, but the X. Fang et al. (2017) model has a significant difference of almost 2000 km. The constants from this model are significantly lower compared to the others, as the shape considered is less flared. They also eliminate crossings where the solar zenith angle is greater than 5°, which we have not done for this study. The IMB models all follow the same trend, with a difference in values of up to 1000 km at times. The N. Edberg et al. (2008) model is consistently higher than the D. Vignes et al. (2000)

and J. G. Trotignon et al. (2006) models, but this is likely due to the contrasting amounts of data that have gone into the creation of these models, as N. Edberg et al. (2008) use the whole Mars Global Surveyor data set. There has not been much modeling carried out on the IMB, and this highlights how variable it can be.

3.2. Position with Respect to the Surface

To look at any variations with respect to the Martian surface, we binned results based on their areographical location in 10° latitude by 10° longitude groups. Results for the terminator distance and normalized terminator distance can be seen for the bow shock in Figures 6(a) and (b), respectively, with the number of crossings within each bin in Figure 6(c). There are gaps present in the northern hemisphere at higher latitudes due to a gap in the orbital coverage from both MEx and MAVEN. In general, terminator distance values are highest near the equator $\pm 30°$, with values ranging between 11,000 and 13,500 km (for the mean R_{TD} case). Toward the poles, values decrease, with the northernmost values being lowest at less than 8000 km. It is worth noting that there is a lack of data points at these latitudes, though, as highlighted in the crossing frequency distribution in Figure 6(c).

Results for the IMB mean terminator distance and mean normalized distance are shown in Figures 6(d)–(e). There is a data gap between $-20°$ and $-50°$, and also at both poles due to orbital constraints of MEx and MAVEN during the study period. Similarly to the bow shock, values are highest across
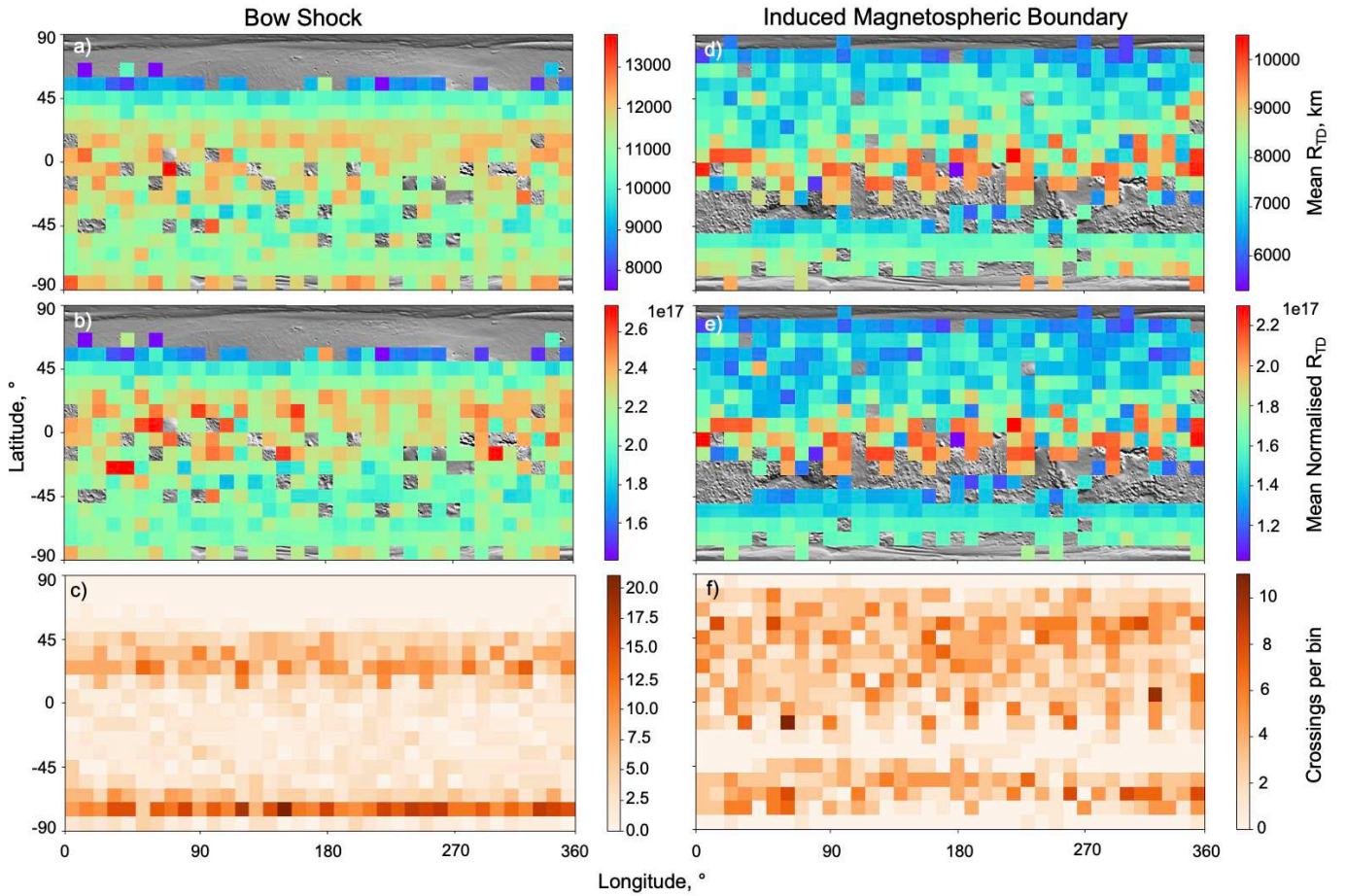
Figure 6. Results for the bow shock (a)–(c) and induced magnetospheric boundary (d)–(f) across the Martian surface for all dayside crossings of MAVEN and Mars Express from 2018 April 1 to November 30, in $10° \times 10°$ bins. (a), (d) Mean fitted terminator distance from Equation (1); (b), (e) normalized (to $r^{2.02}$) mean fitted terminator distance, considering the changing Mars–Sun distance and dynamic pressure; (c), (f) number of boundary crossings within each bin. Base map of the Martian topography for reference to surface features. Topography obtained by the Mars Global Surveyor's Mars Orbiter Laser Altimeter digital elevation model (USGS 2023).

the equatorial region, with values ranging between 8000 and 10,000 km (for the nonnormalized case), decreasing toward the north and south poles. The lowest values of below 6000 km are present at the north pole. Similarly to the bow shock, the crossing frequency per bin decreases at the highest absolute latitudes at the north and south pole (Figure 6(f)).

To ensure there are no space weather influences on our data set, we looked at the solar wind conditions from ASPERA-3 on MEx and SWIA on MAVEN. In general, data from both spacecraft are in reasonable agreement. The values are expected during solar minimum conditions, and there are no solar events causing an increase in density or velocity that were observed by MAVEN or MEx. Neither mission has a continuous solar wind measurement over the study period.

4. Discussion

We consider the study period as a whole, rather than splitting it into stages of dust development for our analysis. This is due to the orbital limitations of both spacecraft meaning global coverage is not achieved in each phase of the dust storm. This influences the distribution of crossings, with a bias of identification where the spacecraft is located at any time. We now analyze each boundary separately below.

4.1. Bow Shock

Considering the rolling mean of the bow shock during the study period (Figure 7), there is no significant variation in the value of the terminator distance; however, when this is corrected for changes in Sun–Mars distance, a negative trend appears. As the storm develops, the normalized terminator distance decreases, and increases slightly as surface conditions return to normal. This follows a similar trend to the IMB, suggesting they are coupled, which is discussed later.

To investigate the influence of the crustal magnetic fields at Mars, we looked at the position of each crossing with respect to the surface, using the J. W. Gao et al. (2021) crustal field model. These locations are shown in Figure 8(a). Crossings are scattered, with some groupings in latitude across all longitudes in both hemispheres ($20°$ to $45°$ in the north and $-68°$ to $-76°$ in the south). The crustal fields are stronger in the southern hemisphere, so we limited crossings to this southern band. The normalized mean terminator distances here are shown in Figure 9. There is some variation in values, but considering the standard deviations, this becomes insignificant; therefore, during this period the bow shock shows no strong influence from the strongest crustal fields in the southern hemisphere, although due to the bias in orbital coverage it is difficult to conclude this globally.
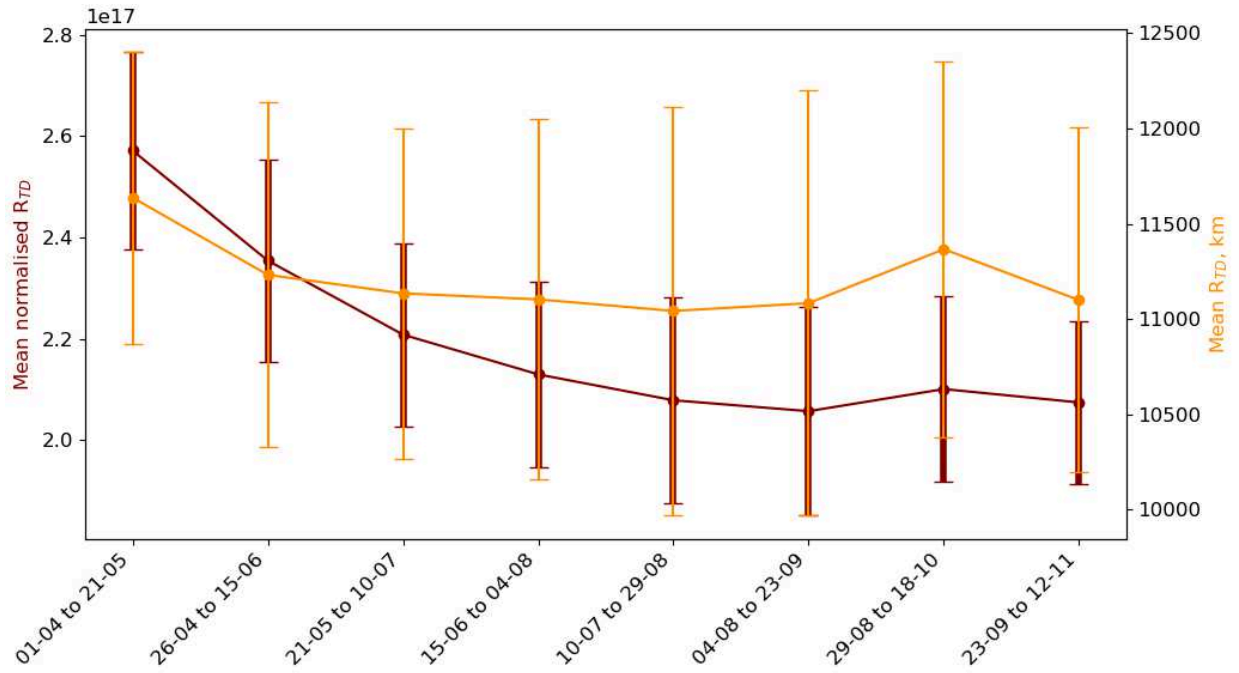
Figure 7. Rolling mean of the fitted and corrected terminator distance, R_{TD}, for the bow shock. Mean calculated every 50 days in 25 day steps from 2018 April 1 to November 30, with error bars of the standard deviation.
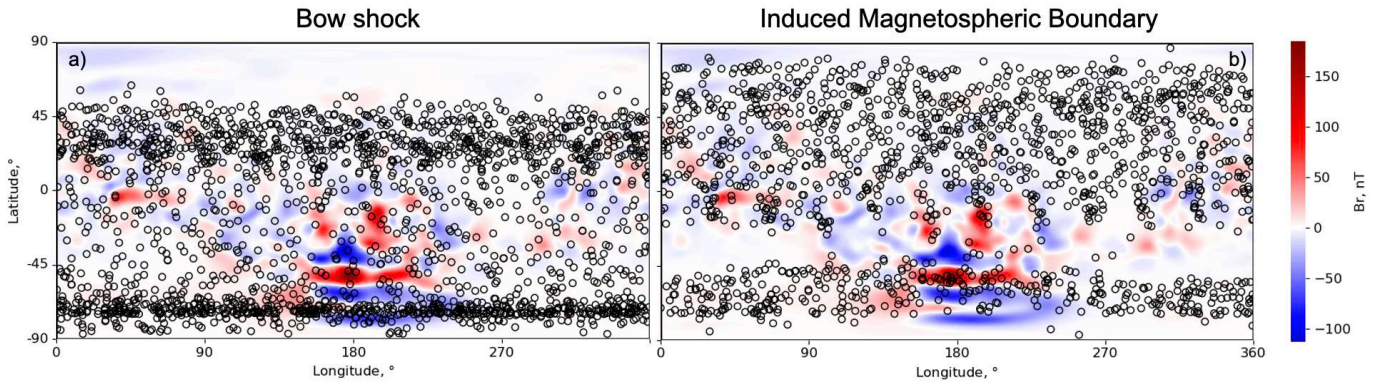

Figure 8. Positions of boundary crossings of MAVEN and MEx from 2018 April 1 to November 30 for the (a) bow shock and (b) induced magnetospheric boundary. Plotted over the radial crustal magnetic field strength at 400 km altitude, given by the Gao model (J. W. Gao et al. 2021).

4.2. IMB

For the IMB, the terminator and normalized values are shown in Figure 10. The trends for both are similar, indicating that the variation in the Sun–Mars distance is not a major influencing factor during this period.

The distribution of IMB crossings with respect to the crustal fields at Mars is shown in Figure 8(b). A band of continuous longitudinal coverage is present from latitudes $-40°$ to $-80°$, including areas from those with no crustal magnetic field strength to some of the strongest crustal fields at the midlongitudes. We limit data to this band to investigate whether the crustal fields are influencing the IMB during this study period.

As well as limiting the data to this areographical region, we also split it by dust storm phase (Table 3). Figure 11 shows that the IMB moves closer to the surface over crustal fields during times of dust activity. Normal behavior of the IMB shows the boundary moving farther from the surface over strong crustal fields (as found by D. H. Crider et al.

2002, 2003; N. Edberg et al. 2008; X. Fang et al. 2017; J. R. Gruesbeck et al. 2018; P. Garnier et al. 2022a, 2022b), but this result agrees with the results of an investigation of the 2007 global dust storm (C. Regan et al. 2024). There is a bias present in the amount of data in each storm phase, which results in the large standard deviation values. This depression over crustal fields is seen to be mainly present during times of dust activity in the atmosphere of Mars. In the pre- and post-storm time periods, values are more stable, although they do not show the typical bulge over crustal field regions that would be expected.

In C. Regan et al. (2024), it is suggested that this feature is caused by the confinement of charged particles over crustal fields reducing ionization rates in comparison to elsewhere on the planet. After seeing this feature again, we suggest a different cause of this signature than that stated in C. Regan et al. (2024). This is due to the past studies not identifying that ionization rates vary across the planet during global storms (M. Felici et al. 2020; V. Mukundan et al. 2021). As
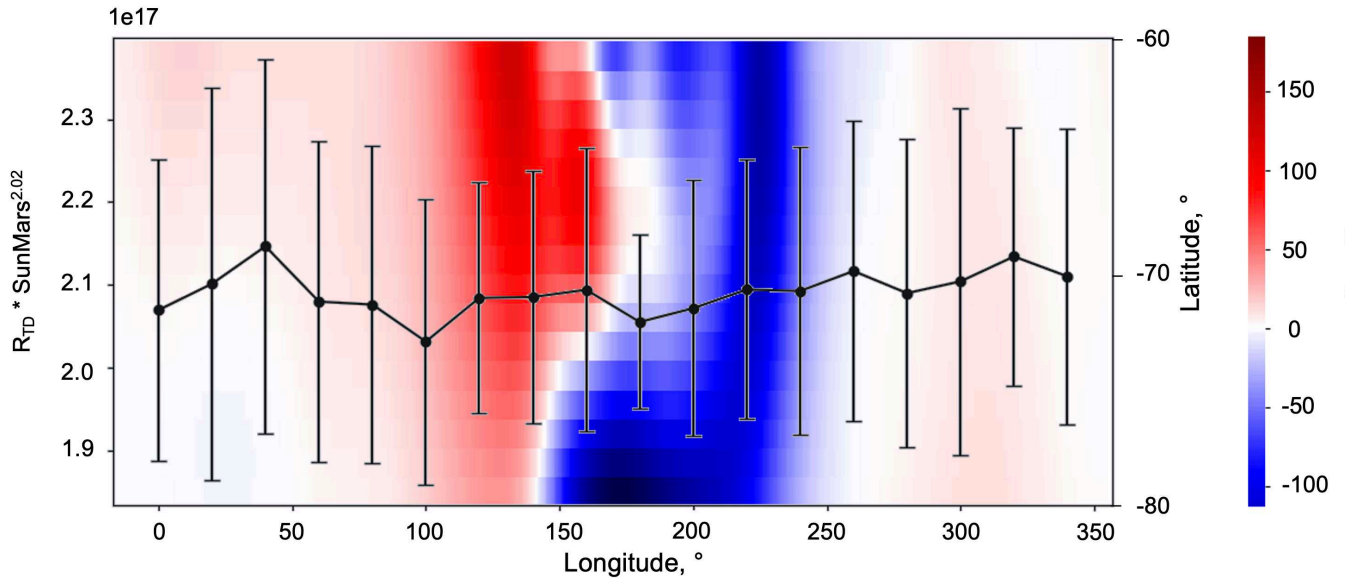
Figure 9. Mean corrected terminator distance of the bow shock, calculated for each 20° longitude interval with latitude limited to −80° to −60°, and error bars of standard deviation plotted over the radial component of the magnetic field at 400 km altitude for this latitude range from the Gao model (J. W. Gao et al. 2021).
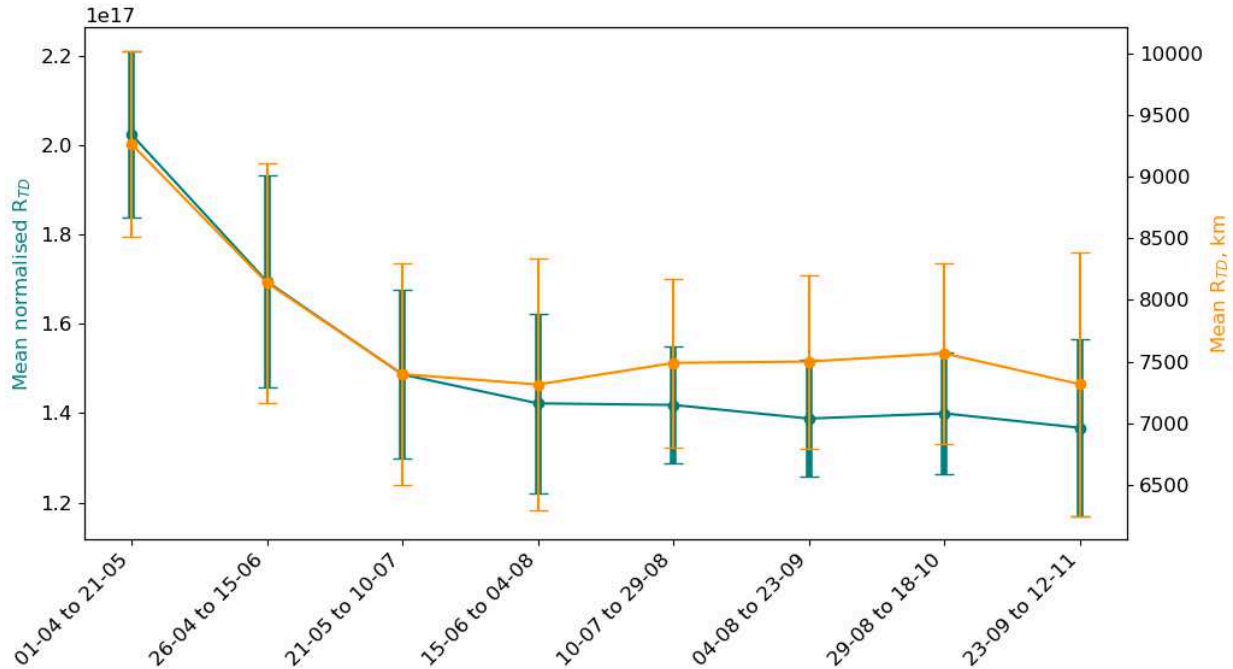

Figure 10. Rolling mean of the fitted and normalized terminator distance, R_{TD}, for the IMB. Mean calculated every 50 days in 25 day steps from 2018 April 1 to November 30, with error bars showing the standard deviation.

Table 3
Phase Split of the 2018 Martian Global Dust Storm

2018 Dates	Dust Storm Phase
Apr 1–May 15	Pre–Global Dust Storm
May 15–Oct 26	Storm Development, Global Storm, and Decay Phase
Oct 26–Nov 30	Post–Global Dust Storm

atmospheric particles are uplifted and ionized due to the dust storm, we suggest they then travel back down toward Mars along magnetic field lines. They then recombine or photodissociate, consequently decreasing the ionospheric pressure in these areas. A decrease in ionospheric pressure allows the IMB to move closer to the planet as the pressure from the magnetosheath dominates. This process is visualized in Figure 12. To further investigate this process, in-depth atmospheric and ionospheric modeling would help understand particle transport processes toward Mars and determine if this is the cause of the IMB depression seen for both the 2018 and 2007 storms. While this signature is consistent with the 2007 study, the strong distinction between dusty and nondusty times in Figure 11 was not expected and provides further evidence of this being a dust storm related feature.

Whether this feature is also present during regional or local dust storms at Mars is currently unknown. Dust storms vary in
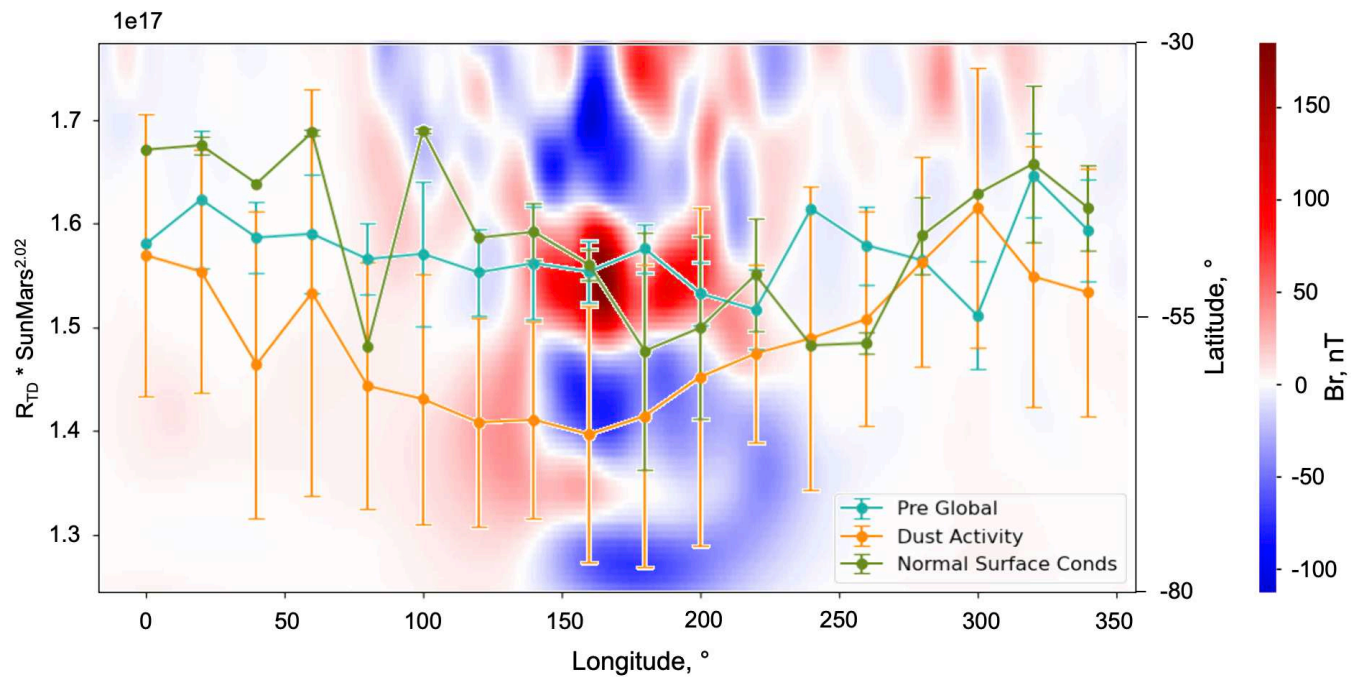
Figure 11. Mean corrected terminator distance of the IMB, calculated for each 20° longitude interval with a latitude limited to −80° to −30°, split into three stages of dust development as outlined in Table 3, with error bars as standard deviation plotted over the radial component of the magnetic field at 400 km altitude for this latitude range from the Gao model (J. W. Gao et al. 2021).
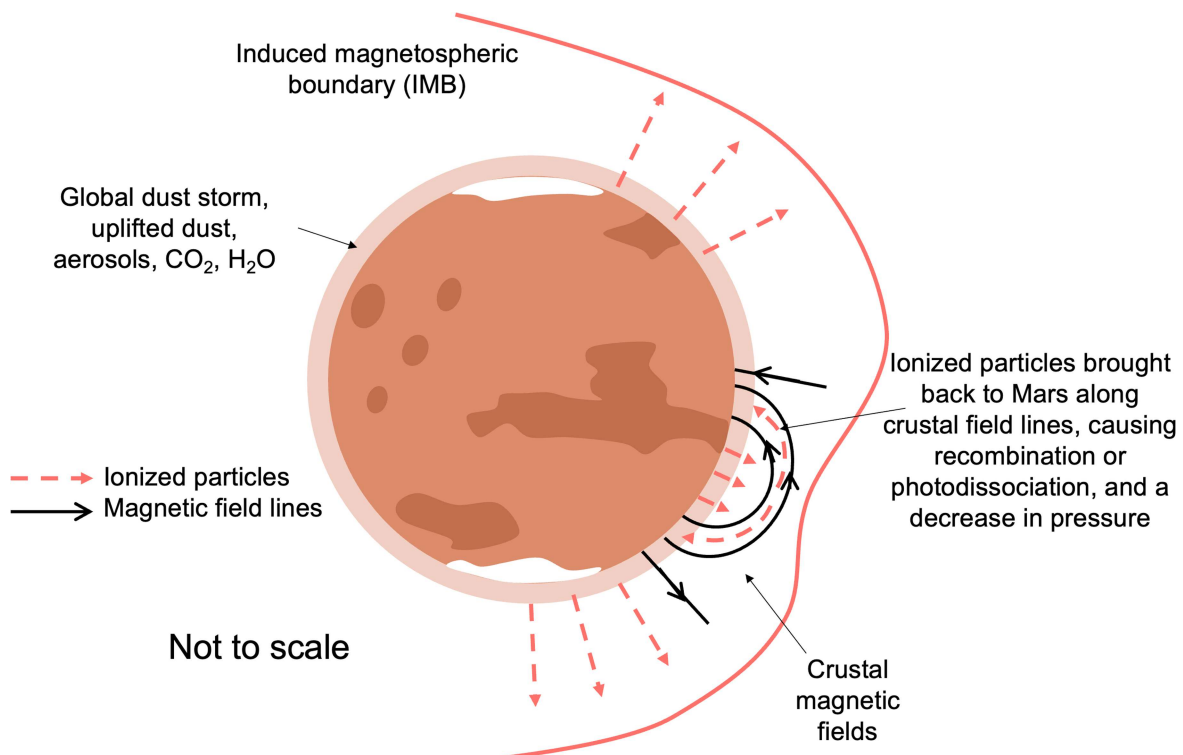

Figure 12. Possible cause of the depression in the induced magnetospheric boundary over crustal fields seen during global dust storms.

size and length but show similarities in their impact on the Martian system. Z. Girazian et al. (2019) found in studies of six events (sizes varying from local to global) that the peak ionospheric altitude increases in all events, showing a significant increase in the upper atmospheric variability. M. Felici et al. (2024) found during regional dust storms in 2021 and 2022 (which occurred in the southern hemisphere)

that ionization rates increased down to altitudes of 80 km, so a depression in the IMB may be present during these events. Investigations into regional storms and their impact on the IMB are beyond the scope of this study.

Solar wind data from both MEx and MAVEN, in addition to a solar wind propagation model from C. Tao et al. (2005, 2015), were analyzed against the model terminator

distance outputs to check there was no influence of solar wind conditions. No dependence was found against the results.

5. Conclusions

Global dust storms at Mars last several months and cause changes in atmospheric and ionospheric compositions. The 2018 storm was no exception to this. The impact on the magnetosphere of Mars is present as an increase in boundary variability of the bow shock and IMB. MAVEN and MEx crossings introduce orbital bias in our data as their orbits favor certain areas of Mars over the study period. However, between both spacecraft over a period of 8 months we get reasonable coverage of dayside boundary crossings with respect to the Martian surface. Looking at both boundaries generally, when correcting for the change in Sun–Mars distance, they both move closer to the surface as the dust storm develops, indicating they are coupled. Although there is not a continuous areographical coverage of the Martian surface over the study period, both boundaries have a high concentration of crossings over a specific latitude range, allowing comparison to be done over areas of strong and weak crustal fields. The bow shock shows no relationship to the strongest crustal fields in the southern hemisphere, but the IMB dips over crustal magnetic fields during times of dust activity. Previous studies have found that the boundary bulges here, but this depression is consistent with the signature found in the 2007 global dust storm study. We suggest this signature is caused by the ionized atmospheric particles being scattered by crustal magnetic field lines where they travel back toward Mars, recombining and therefore reducing ionospheric pressure in this area. Further study is needed to confirm whether this behavior of the IMB is consistent with the occurrence of global dust storms. In particular, study of the magnetic topology of the crustal fields and modeling of atmospheric and ionospheric particles would enable further investigation into this cause. This is beyond the scope of this study. The main limitation on this study is the orbital bias presented by MAVEN and MEx, so additional spacecraft that are able to identify plasma boundary crossings would fill this gap for further study during the next Martian global dust storm.

Acknowledgments

ORCID iDs

Catherine E. Regan ⓘ https://orcid.org/0000-0001-8784-5919
Andrew J. Coates ⓘ https://orcid.org/0000-0002-6185-3125
Anne Wellbrock ⓘ https://orcid.org/0000-0002-2861-7999
Geraint H. Jones ⓘ https://orcid.org/0000-0002-5859-1136
Beatriz Sánchez-Cano ⓘ https://orcid.org/0000-0003-0277-3253
František Němec ⓘ https://orcid.org/0000-0002-3233-2718
Mats Holmström ⓘ https://orcid.org/0000-0001-5494-5374

References

Barabash, S., Lundin, R., Andersson, H., et al. 2006, SSRv, 126, 113
Bertucci, C., Duru, F., Edberg, N., et al. 2011, SSRv, 162, 113
Burne, S., Bertucci, C., Mazelle, C., et al. 2021, JGRA, 126, e28938
Cardesin-Moinelo, A., Godfrey, J., Grotheer, E., et al. 2024, SSRv, 220, 25
Chaffin, M. S., Chaufray, J. Y., Stewart, I., et al. 2014, GeoRL, 41, 314
Connerney, J., Espley, J., Lawton, P., et al. 2015, SSRv, 195, 257
Crider, D. H., Acuña, M. H., Connerney, J. E., et al. 2002, GeoRL, 29, 9
Crider, D. H., Vignes, D., Krymskii, A. M., et al. 2003, JGRA, 108, 1461
Edberg, N., Brain, D., Lester, M., et al. 2009, AnGeo, 27, 3537
Edberg, N., Lester, M., Cowley, S., & Eriksson, A. 2008, JGRA, 113, A08206
Fang, X., Ma, Y., Masunaga, K., et al. 2017, JGRA, 122, 4117
Farahat, A., Mayyasi, M., Withers, P., Dayeh, M. A., & Abuelgasim, A. 2021, JGRE, 126, e2021JE006868
Fedorova, A. A., Bertaux, J., Betsis, D., et al. 2018, Icar, 300, 440
Fedorova, A. A., Montmessin, F., Korablev, O., et al. 2020, Sci, 367, 297
Felici, M., Segale, J., Withers, P., et al. 2024, Icar, 424, 116089
Felici, M., Withers, P., Smith, M. D., et al. 2020, JGRA, 125, e27083
Gao, J. W., Rong, Z. J., Klinger, L., et al. 2021, E&SS, 8, e01860
Garnier, P., Jacquey, C., Gendre, X., et al. 2022a, JGRA, 127, e2021JA030147
Garnier, P., Jacquey, C., Gendre, X., et al. 2022b, JGRA, 127, e2021JA030146
Girazian, Z., Luppen, Z., Morgan, D., et al. 2019, JGRE, 125, e2019JE006092
Gruesbeck, J. R., Espley, J. R., Connerney, J. E., et al. 2018, JGRA, 123, 4542
Guzewich, S. D., Lemmon, M., Smith, C. L., et al. 2019, GeoRL, 46, 71
Halekas, J. S., Taylor, E. R., Dalton, G., et al. 2015, SSRv, 195, 125
Hall, B., Lester, M., Sánchez-Cano, B., et al. 2016, JGRA, 121, 474
Hall, B., Sánchez-Cano, B., Wild, J., Lester, M., & Holmström, M. 2019, JGRA, 124, 4761
Jakosky, B. M., Lin, R. P., Grebowsky, J. M., et al. 2015, SSRv, 195, 3
Kass, D. M., Schofield, J. T., Kleinböhl, A., et al. 2019, GeoRL, 46, e2019GL083931
Linzmayer, V., Němec, F., Němeček, Z., & Šafánková, J. 2024, AdSpR, 73, 6298
Mitchell, D. L., Mazelle, C., Sauvaud, J. A., et al. 2016, SSRv, 200, 495
Montabone, L., Spiga, A., Kass, D. M., et al. 2020, JGRE, 125, e2019JE006111
Mukundan, V., Thampi, S. V., Bhardwaj, A., & Fang, X. 2021, JGRE, 125, e2021JE006823
Niu, D. D., Cui, J., Wu, S. Q., et al. 2021, JGRE, 126, e2020JE006679
Němec, F., Linzmayer, V., Nemecek, Z., & Safrankova, J. 2020, JGRA, 125, e2020JA028509
Peter, K., Patzold, M., Montabone, L., et al. 2023, Icar, 400, 115565
Qin, J. F., Zou, H., Lee, Y., et al. 2022, JGRE, 127, e2022JE007297
Regan, C., Coates, A., Lester, M., et al. 2024, PSJ, 5, 130
Roeten, K. J., Bougher, S. W., Benna, M., & Elrod, M. K. 2022, Icar, 382, 115006
Rossi, L., Vals, M., Montmessin, F., et al. 2021, GeoRL, 48, e2020GL090962
Sánchez-Lavega, A., del Rìo-Gaztelurrutia, T., Hernández-Bernal, J., & Delcroix, M. 2019, GeoRL, 26, 6101
Tao, C., Budnik, E., Bouchemit, M., et al. 2015, Solar Wind In Situ Parameters Propagated from the Earth to Mars, v1, Ovgso, doi:10.6096/2001
Tao, C., Kataoka, R., Fukunishi, H., Takahashi, Y., & Yokoyama, T. 2005, JGRA, 110, A11208
Trotignon, J. G., Mazelle, C., Bertucci, C., & Acuñ, M. H. 2006, P&SS, 54, 357
USGS 2023, Mars MGS MOLA DEM 463m, https://astrogeology.usgs.gov/search/map/mars_mgs_mola_dem_463m
Venkateswara Rao, N., Leelavathi, V., Mohanamanasa, P., Haider, S., & Rao, S. 2019, JGRA, 124, 3007
Vignes, D., Mazelle, C., Rme, H., et al. 2000, GeoRL, 27, 49
Wang, M., Xie, L., Lee, L., et al. 2020, ApJ, 903, 125